Available online at www.sciencedirect.com

ScienceDirect

Advances in Space Research 61 (2018) 2673–2679

ADVANCES IN SPACE RESEARCH
(a COSPAR publication)

www.elsevier.com/locate/asr

Development and verification of an innovative photomultiplier calibration system with a 10-fold increase in photometer resolution

Shyh-Biau Jiang [a,b], Tse-Liang Yeh [a,b], Li-Wu Chen [b,*], Jann-Yenq Liu [c], Ming-Hsuan Yu [b], Yu-Qin Huang [a], Chen-Kiang Chiang [b], Chung-Jen Chou [b]

[a] Institute of Mechanical Engineering, National Central University, Taoyuan City 32001, Taiwan
[b] Institute of Opto-Mechatronics Engineering, National Central University, Taoyuan City 32001, Taiwan
[c] Institute of Space Science, National Central University, Taoyuan City 32001, Taiwan

Received 24 January 2017; received in revised form 27 February 2018; accepted 28 February 2018
Available online 9 March 2018

Abstract

In this study, we construct a photomultiplier calibration system. This calibration system can help scientists measuring and establishing the characteristic curve of the photon count versus light intensity. The system uses an innovative 10-fold optical attenuator to enable an optical power meter to calibrate photomultiplier tubes which have the resolution being much greater than that of the optical power meter. A simulation is firstly conducted to validate the feasibility of the system, and then the system construction, including optical design, circuit design, and software algorithm, is realized. The simulation generally agrees with measurement data of the constructed system, which are further used to establish the characteristic curve of the photon count versus light intensity.

Keywords: Photomultiplier calibration; Airglow; Optical attenuator

1. Introduction

The paper goal is to build a calibration system to calibrate airglow instruments with high sensitivity photomultipliers. In the visible spectral region, airglow of 630.0 nm emissions can be observed from the ground and satellites. Scientists (Barbier, 1959; Porter et al., 1974; Mendillo et al., 1997; Kubota et al., 2001; Rajesh et al., 2010; Liu et al., 2011) often conducted 630.0 nm airglow ground-based experiments observing gravity waves, traveling ionospheric disturbances, and plasma depletions. On the other hand, satellite observations give a unique view of the global and/or the altitude-latitude distribution of airglow emission in nighttime with very high spatial resolution (*cf.* Rajesh et al., 2009, 2014). The 630.0 nm measurements have the advantage that the intensity is related to the plasma density and is also sensitive to the altitude variations of the ionosphere (Peterson et al., 1966; Nelson and Cogger, 1971; Bittencourt and Sahai, 1979; Herrero and Meriwether, 1980; Link and Cogger, 1988).

Bird et al. (1994) proposed a method for correcting high-sensitivity photomultiplier tubes. The proposed method uses a monochromatic UV light source as the test light source, and a photodiode as the standard optical sensor. In this method, the high-intensity photoelectric properties of the photodiode are first calibrated, and then a linear extrapolation of its low-intensity photoelectric properties is calculated. Finally, the optoelectronic properties of the low-intensity section of the diode can be used as a standard

* Corresponding author.
E-mail address: smallwind323@hotmail.com (L.-W. Chen).

https://doi.org/10.1016/j.asr.2018.02.039
0273-1177/

for calibrating photomultiplier tubes (Bird et al., 1994). Abbasi et al. (2010) built the IceCube Neutrino Observatory in Antarctica, used a photomultiplier group matrix as a sensor group, and proposed a calibration method for the observatory.

The key component of airglow instruments/payloads is a photomultiplier tube before CCD cameras became kind of a standard. This paper is to describe a calibration system for photomultipliers, which allows us to find the characteristic curve of the photon count versus light intensity, and correctly observe airglow emissions for tomography reconstruction (Hsu et al., 2009; Liu et al., 2010; Yeh et al., 2012). Here, we take the 630.0 nm emission as an example. Owing to the airglow intensity being rather low, a highly sensitive detector will be required. Photomultiplier tubes are the most sensitive detectors that are commercially available. However, a photomultiplier tube is very difficult to be calibrated, because any intense test light source could easily damage it. By contrast, optical power meters have been commonly used for optical calibration, and unfortunately, their sensitivity is too low to be employed observing airglow emissions. To resolve these difficulties, we construct a calibration system with a 10-fold optical attenuator. The system enables that after light from the light source has passed through the attenuator, two different intensities of light with the ratio of 1–10 can be produced for calibration. For the calibration, the intense and faint lights shine on the optical power meter and the photomultiplier, respectively. A simulation is conducted to confirm the feasibility of the proposed calibration system. After the confirmation, a calibration system is constructed. Finally, measurement data are used to obtain the photon count-light intensity characteristic curve.

2. Photomultiplier tube

A photomultiplier tube consists of an input window, a photocathode, a plurality of dynodes, and an anode. It produces a surge of electron flow upon the incident of a photon at the cathode. Applying negative distributed high voltage to the cathode and a cascade of dynodes the number of electrons ejected from the cathode by a photon is multiplied geometrically by each dynode resulting in an amplification of 5 to 6 order of magnitude to produce a pulse current output at the anode of time within nanoseconds. Therefore, it is very sensitive with very high signal to noise ratio and big dynamic range. Its optical response may extend from the infrared region to the ultraviolet region depending on the photocathode material and the manufacture of tubes.

3. Calibration system design

We develop a calibration system to measure the deviations from linearity of our photomultiplier tube based photon counting system. 630.0 nm was targeted as an easier example for concept demonstration. A LED of spectral range 580–680 nm was applied as the light source. To single out 630.0 nm light to target at the characteristic airglow, a 630 ± 1 nm filter was installed. A high sensitivity optical power meter with resolution down to 1 pW was employed as the standard reference measuring the actual irradiance power on the sensing area. However, the resolution of the optical power meter is still much coarser than the sensitivity of the photon counting system that it cannot be applied directly as the calibration reference standard for comparison. We designed an adjustable optical attenuator to produce two light intensity variation patterns with fixed proportionality and reproduceable position dependence. The light shutter with 1-hole and 10-hole design provides different light sources with an order of magnitude ratio in the intensity. The two sensors of very different sensitivities can be driven by the two different light sources for comparison. Then, the data can be used to construct a characteristic calibration curve.

A functional block diagram of the calibration system is shown in Fig. 1. The radiant light from the source is converted into a light beam parallel to the optical axis of the platform by a plano-convex lens. The intensity distribution over its cross section is $i_0(r, \theta)$, where r is the distance from the optical axis and θ is the angle by which the attenuator rotates. Parallel light passes through a rotating adjustable optical attenuator to produce a light spot exiting the attenuator. The intensity distribution of the penetrating light exiting the attenuator disk is $i(R, \Theta)$, where radius R and angle Θ are the polar coordinates on the exit plane of the attenuator centered at the optical axis. The attenuated light is then imaged onto the light sensing area through the focusing lens 2 and the 630 nm narrow band filter. There, the total irradiance incident on the sensor is, thus, a function $I(\Theta)$ of the angular position Θ of the attenuator. Using either the photon counting system or the optical power meter as the sensor, we can correlate their measurement of $I(\Theta)$, we obtain the calibration function to convert the photon counting rate to the benchmarked photonic power, and, thus, the column intensity in rayleighs along the line of sight. To conduct a calibration, we program the optical attenuator controller to scan through the rotation angle Θ for a large range of adjustable intensity attenuation. Simultaneously, we record the measurement data indexed by the angular position Θ. So that we obtain the characteristic curve of the photon count $P(\Theta)$ versus light intensity $W(\Theta)$. A human–machine computer interface is designed to automate the scan: measuring, recording $P(\Theta)$ and $W(\Theta)$, and the function $W(P)$ of the photon counting system under test.

The top panel of Fig. 2 shows that an optical mechanism consists of a single-frequency light source, light-parallelizing lens, adjustable optical attenuator, and light-focusing lens. The light source used in this system is a red LED (Model 597-3002-507F, Dialight), whose spectral range is 580–680 nm. The filter used (model 630NB2) is obtained from Omega Optical. Both the light-parallelizing and light-focusing lenses are done by plano–

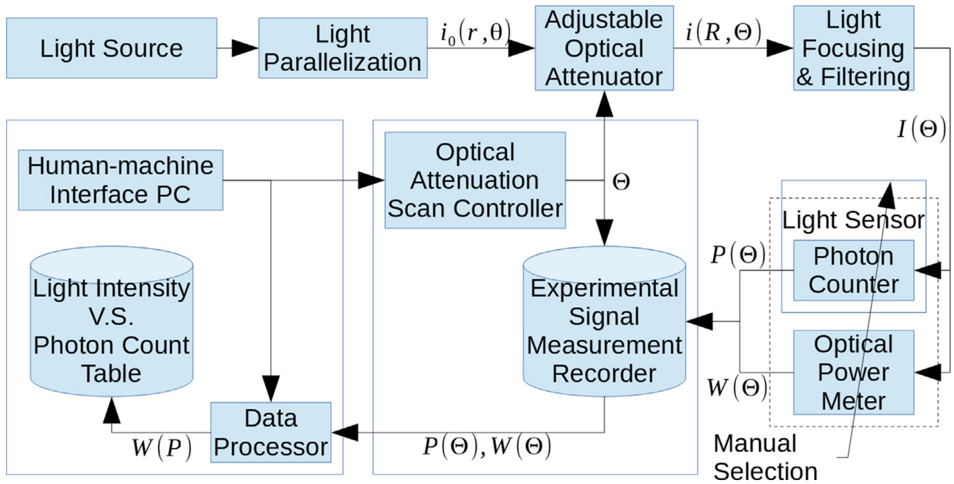

Fig. 1. Functional block diagram of the calibration system.

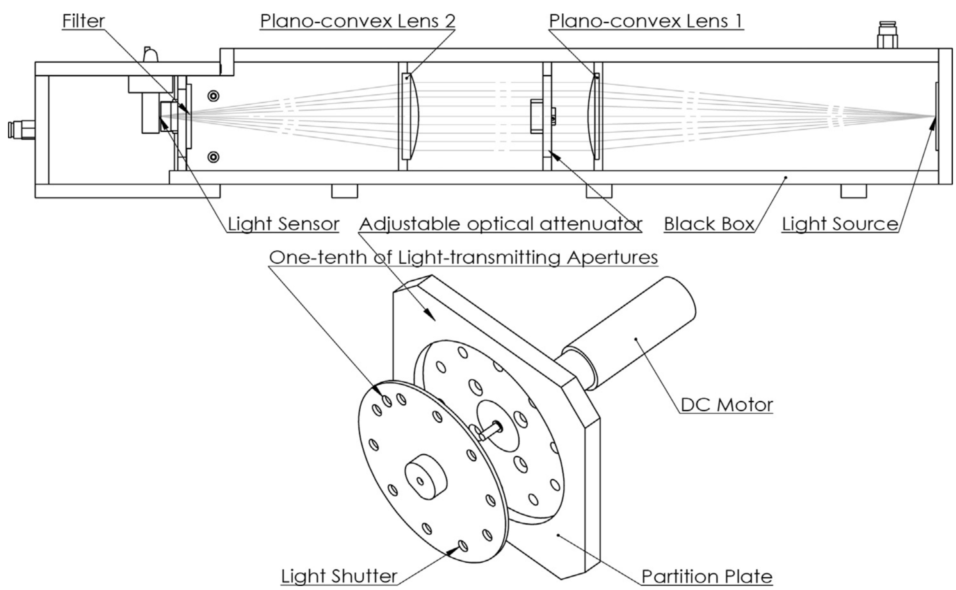

Fig. 2. Optical mechanical design of the calibration system.

convex lenses. The light source is placed at the focal point of the light-parallelizing lens to mimic airglow emissions from far away and to make the light on each hole being uniform and equal, while on the other side the light sensor is placed at the focal point of the light-focusing lens to ensure the through-hole light to be received by the sensor. The lower panel of Fig. 2 displays that the adjustable optical attenuator comprises a stationary partition plate, a rotating light shutter, and a motor. The partition plate is fixed in the black box with ten 3 mm diameter light transmitting holes. We need to consider the number and size of holes that can be accommodated in the light shutter, convenience in manufacture, in data analysis, and in drawing position correlation. One major concern should be the choice of a distribution ratio which would bring the relative resolution of the optical power meter to be comparable to that of the photon counting system so that the calibration can be made with the best resolution. The holes are distributed at equally spaced angle on a circle around the center axis of the partition plate. In parallel and in sliding proximity to the partition plate, we place a co-axial circular light shutter disk with eleven light transmission holes. 10 of the light transmission holes are equally spaced on a circle the same as those in the partition plate so that the two sets can line up to form a transmission aperture of 10 holes. Thus, 10 periodic irradiance patterns, varying from the total darkness to a maximum brightness, can be produced by rotating the light shutter disk in a full rotation. The 11th light transmission hole of the same diameter in the light shutter disk is located on the same circle, midway between one pair of the other holes. When the light shutter rotates, the 11th hole would line up with only one at each time of the light transmission holes in the partition plate. Thus, forms an aperture profile of a magnitude in the same fraction as the ratio of the number of holes 1/10. As the light shutter is rotated by the motor, the overlapping area of the light transmission is depends on angle of rotation can be calculated analytically. Specially shaped holes may lead to a more linear variation, but circular holes are the easiest to manufacture with good accuracy. When the holes are aligned, the light transmittance reaches a maximum. While position is offset more than the diameter of a hole, transmittance is reduced to zero.

A simulation of one full rotation of 11-hole shutter that corresponds to the 10-hole partition plate that follows refers to the scheme just described is shown in Fig. 3, where 11-hole shutter and 10-hole partition plate refer to the rotating and fixed parts of the adjustable optical attenuator. In each full rotation, the light transmittance profile cycles 10 times through the high and low peaks. The profiles are supposed left and right symmetric to each point of zero and peak. We compute the average over these 10 cycles of the repetitive angular function. Particularly, the overlapping of the 11th aperture with each one of the 10 holes in the partition plate, the light transmittance profile is the same function of the angular position that of the 10 holes with 10 holes. Therefore, the small peak profile has a fixed ratio with the large peak profile at corresponding angular position. Thus, the data over the small peak profile can be corresponded to that over the large peak profile for calibration.

A $77 \times 80 \times 450$ mm rectangular black box which is assembled from aluminum plates with a light absorbing matte black surface treatment is designed and constructed to encapsulate the optical components and the devices under test. A light source is mounted at one end, and a manually replaceable optical sensor to be tested, either the optical power meter or the photon counting system is mounted at the other end (Fig. 4). The rotating adjustable optical attenuator is installed in the middle of the rectangular box. The plano-convex lenses are mounted at the positions corresponding 1/4 and 3/4 of the length of the box. The light shutter of the adjustable optical attenuator is driven by a small DC motor with an 1 pulse per step (pps) angle encoder and 4096:1 reduction gearbox under the position control of our ASA-DSMD DC motor driver to achieve 0.35°/step angular positioning. With this resolution, each large and small peak profiles can be sampled fine enough for a smooth calibration curve.

The optical power meter is NOVA2 (OPHIR) and the sensing probe is PD300-UV. The photon counting system for 630.0 nm is composed of a R4632 photomultiplier tube (Hamamatsu), matched preamp, discriminator, and a prescaler of 10. The prescaler is needed to match up to the photonic pulse width for maximal counting performance. To carry out the calibration procedure automatically, an AVR-ATmega128 based ASA-M128 (see: http://www.ASArobot.com/ASA-M128.html) micro controller is used as the dedicated calibration system controller. This procedure is carried out once with the photon counting system under test for $P(\Theta)$ and another once with the optical power meter reference for $W(\Theta)$.

In the data post processing, we first observe the measurement data. Because of saturation in part of the $P(\Theta)$ curve, the 1-hole transmission must be used. We horizontally shift the $W(\Theta)$ curve so that its 10-hole peak center aligns with the center of the 1-hole peak of the $P(\Theta)$ curve, then the optimal sensing value of the photometer corresponds to the optimal sensed value of the photomultiplier. After shifting, the luminous flux ratio of each pair of $W(\Theta)$ and $P(\Theta)$ is 10:1. At the same Θ angle, where $P(\Theta)$ is the vertical coordinate and $W(\Theta)$ horizontal is the coordinate, it is possible to establish the characteristic curve of the photon count versus light intensity $W(P)$.

4. Data analysis and results

We want to establish the correlation between the photonic pulse counting rate and the power measurement by a standard reference optical power meter. But the photomultiplier tube and the optical power meter have their zero offsets and temperature drift characteristics, therefore, we need to document their dark count and dark measurement in total darkness environment as well as their drift after power turn on to be sure of the time needed for warm up to reach thermal stability. Besides, the warm up time of the light source need to be confirmed too. The thermal noises of the photomultiplier tube as well as that of the optical power meter were measured separately to determine their zero offsets. The data indicate that the average of the dark count of the photomultiplier tube is 61.90 counts/s with standard deviation 9.2 counts/s, while the standard error of mean is 0.2876 counts/s as shown in Fig. 5(a). The average of the thermal noise measurement by the opti-

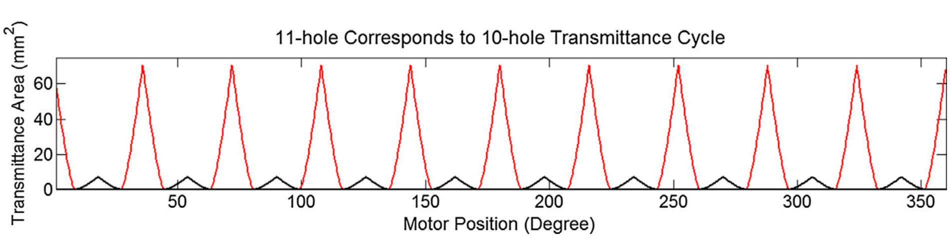

Fig. 3. Simulation of 11-hole shutter that corresponds to the 10-hole partition plate; each rotation of the light shutter has 10 variations of light transmission in its cycle. The red curve is 10-hole transmittance area, and the black curve is 1-hole transmittance area. (For interpretation of the references to colour in this figure legend, the reader is referred to the web version of this article.)

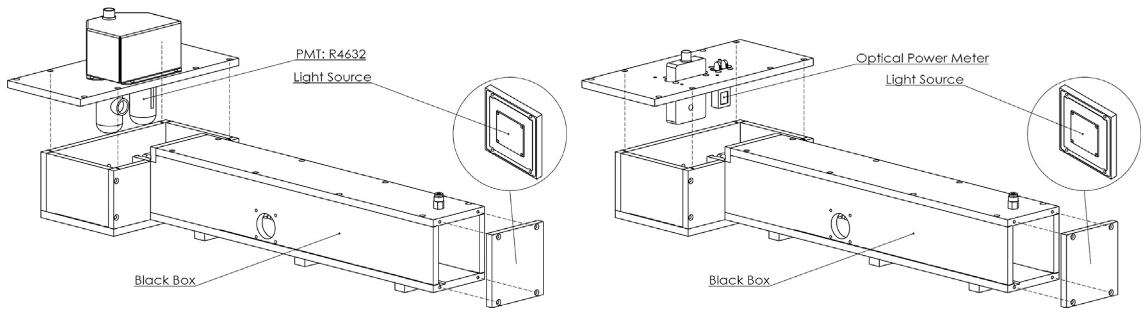

Fig. 4. Optical black box designed for the calibration system. At the right end mounted the light source, and the other end the fit to mount the optical filter with different optical sensors – either an optical power meter or the photon countering system to be calibrated.

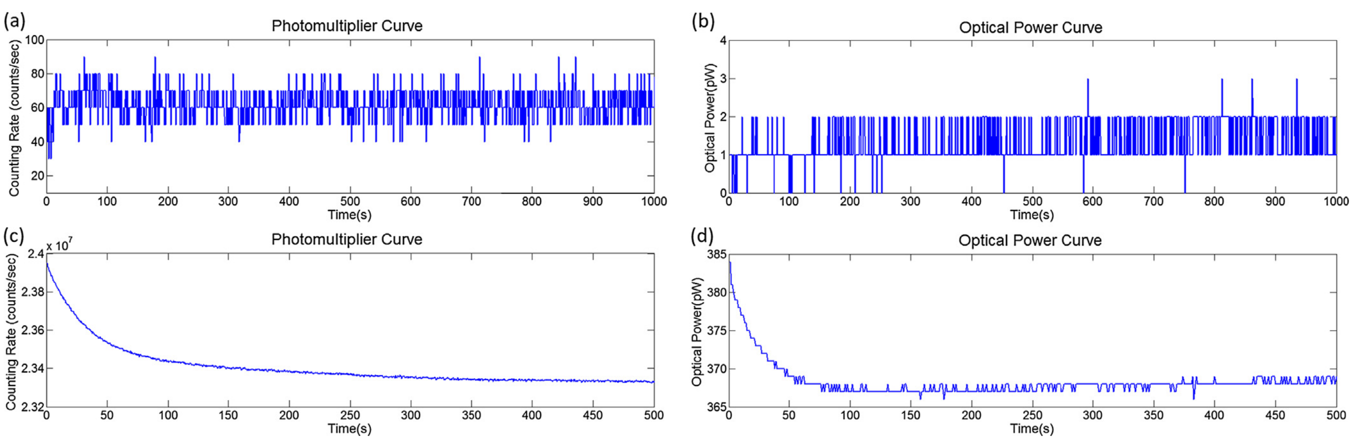

Fig. 5. Figure (a) and (b) are the dark ambient zero offset measurement data of photon multiplier tube and optical power meter, respectively. Figure (c) and (d) are the light source warm up time and thermal stability measurement data of photon multiplier tube and optical power meter, respectively.

cal power meter is 1.34 pW with standard deviation 0.52 pW, while the standard error of mean is 0.0162 pW as shown in Fig. 5(b). The warm up time variation curve of the intensity of the light source under constant voltage drive at a constant attenuator transmittance was measured by the photomultiplier tube as well as the optical power meter to determine the warm up time and the extent of thermal stability. The measured photomultiplier data curve revealed that the photon counting rate at the beginning of the light source turn on is 2.4×10^7 cps. The measurement decreased steadily to reach a steady level 2.3×10^7 cps after 350 s of warm up as shown in Fig. 5(c). As shown in Fig. 5 (d), the power read out by the optical power meter is 384 pW at the initial turn-on. Subsequently, the value dropped progressively to reach the steady state after 100 s when the value has declined to 368 pW. For the calibration process, the warm up time is set to 350 s to ensure that the light source as well as the two sensors all reaches their steady state begins.

The measurement data of the photomultiplier tube and the optical power meter (Fig. 6(a) and (b)) are obtained according to the measurement procedures described above. The post processing results are presented in Figs. 6(c) (d) and 7. As shown in Fig. 6(b), the $W(\Theta)$ curve has two peaks, one high and one low, which repeat throughout the cycle. The high peak line for the 10-hole light transmission range has high resolution, whereas the low-peak line for the 1-hole light transmission range has poor resolution. In 10 repeating 10-hole transmission ranges, the shapes of the curves were similar but not identical. This is because although the similar light hole overlap geometry can theoretically overcome the effect of light source direction nonuniformity, small eccentricities in the light source, lens, and sensor position produce minute differences, also diffraction and internal reflection effects in the holes are likely to contribute to some data scatter. In addition to the repetition of the waveform cycles, each peak also had symmetrical right–left characteristics because the overlapping areas of the apertures are left–right symmetrical. To reduce the influence of the positional eccentricity of the light source, lens, and sensor, every overlapping range of a full rotation of measurement data was divided, producing 10 equal parts. The average values of these 10 segments of data were then calculated as shown in Fig. 6(d). Notably, the symmetry of the peak can be used to calculate the symmetrical data mean, and thus improve the accuracy of the data.

As shown in Fig. 6(a), when the light intensity was saturated, excessively intensive photon incidents produced pulse pile-up. Thus, the top of the $P(\Theta)$ curve showed concave deformation. Because the 10-hole overlapping range of the $P(\Theta)$ curve was not usable, we used the 1-hole over-

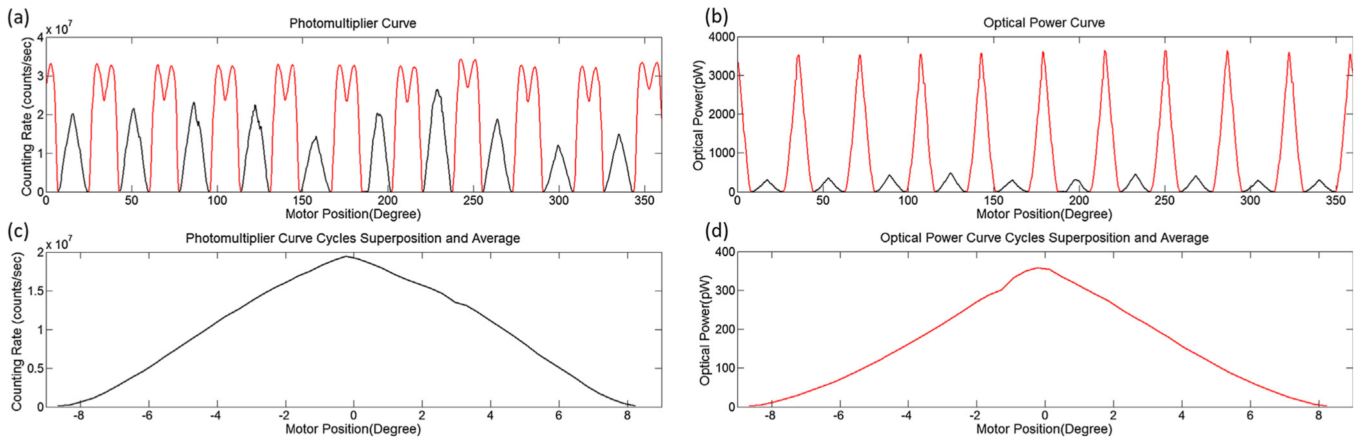

Fig. 6. (a) The raw photomultiplier response curve. (b) The raw optical power meter response curve. (c) Averaged representative photomultiplier responses to the single hole transmittance profile. (d) Averaged representative optical power meter responses to the single hole transmittance profile.

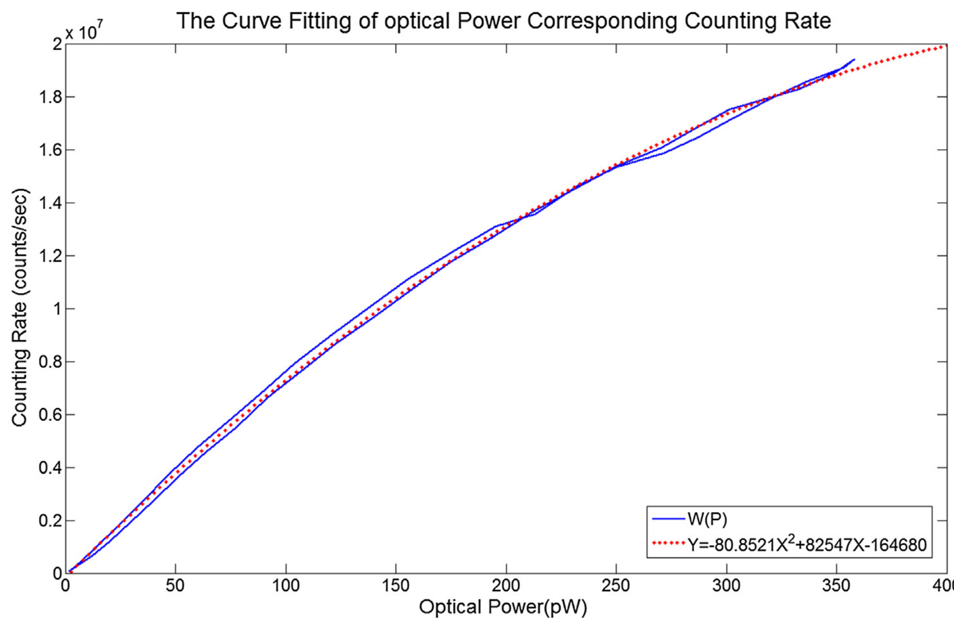

Fig. 7. The $W(P)$ curve in blue line and the quadratic polynomial fit in red dashed curve. (For interpretation of the references to colour in this figure legend, the reader is referred to the web version of this article.)

lapping range. As we did with the $W(\Theta)$ curve, we divided the $P(\Theta)$ curve into 10 segments and then calculated the average of the 10 segments to reduce the effects of nonuniformity and eccentricity as shown in Fig. 6(c). The overall symmetry of the $P(\Theta)$ curve was also averaged to achieve higher accuracy.

As shown in Fig. 7, blue curve, through the data post processing step described above, we shifted the 10-hole overlap region of the $W(\Theta)$ curve to align with the 1-hole overlap region of the $P(\Theta)$ curve at each corresponding motor step, and finally obtained the one-to-one calibration curve of $W(P)$ correlating the optical power values that correspond to photon counting rates. We can fit a second order polynomial to this calibration curve to obtain the optical power X corresponding to each photon counting data Y as shown in Fig. 7, red dashed curve, where X is the optical power in pico Watt (pW) and Y is the photon count rate in cps.

$$Y = -80.8521X^2 + 82547X - 164680$$

5. Conclusions

This paper has described an innovative calibration system that can improve the resolution of an optical power meter by a factor of 10 to calibrate the photomultiplier tube. The proportionality can be adjusted by altering the number of overlapping holes to obtain a different sensitivity ratio between the two detection systems to be compared. This system can calibrate photomultiplier tube based photon counting instruments, and establish a quadratic polynomial approximation formula for the associated characteristic curve. The measurements confirm that the constructed calibration system has the ability to increase the effective resolution of the optical power meter. In short, the system is capable to calibrate the photomultiplier tube based photon counting system. Vice versa, the constructed system can also be used to verify the quality of the power meter against the very good linearity of the photon counting system at low intensity levels.

Acknowledgements

The authors wish to thank the reviewers for their useful comments and suggestions, which significantly improve the paper presentation. This study is supported by Taiwan Ministry of Science and Technology with grants MOST106-2119-M-008-020 and MOST105-2119-M-008-026, and partially by the Aim For The Top University Project grants NCU105G906-18 and NCU104G906-15 at National Central University in Taiwan.

References

Abbasi, R., Abdou, Y., Abu-Zayyad, T., et al., 2010. Calibration and characterization of the IceCube photomultiplier tube. Nucl. Instrum. Methods Phys. Res. A 618, 139–152. https://doi.org/10.1016/j.nima.2010.03.102.

Barbier, D., 1959. Recherches sur la raie 6300 de la luminescence atmospherique nocturne. Ann. Geophys. 15, 179–217.

Bird, D., Corbató, S., Dai, H.Y., et al., 1994. The calibration of the absolute sensitivity of photomultiplier tubes in the High Resolution Fly's Eye Detector. Nucl. Instrum. Methods Phys. Res. A 349, 592–599. https://doi.org/10.1016/0168-9002(94)91230-0.

Bittencourt, J.A., Sahai, Y., 1979. Behavior of the [OI] 6300 Å emission at the magnetic equator and its reaction to the vertical ExB drift velocity. J. Atmos. Sol. Terr. Phys. 41, 1233–1239.

Herrero, F.A., Meriwether, J.W., 1980. 6300 Å airglow meridional intensity gradients. J. Geophys. Res. 85, 4194–4204.

Hsu, M.L., Rajesh, P.K., Liu, J.Y., et al., 2009. Ionospheric electron density concurrently derived by TIP and GOX of FORMOSAT-3/COSMIC. Terr. Atmos. Ocean. Sci. 20 (1), 207–214.

Kubota, M., Fukunishi, H., Okano, S., 2001. Characteristics of medium- and large-scale TIDs over Japan derived from OI 630-nm nightglow observation. Earth Planets Space 53, 741–751. https://doi.org/10.1186/BF03352402.

Link, R., Cogger, L.L., 1988. A reexamination of the OI 6300 Å nightglow. J. Geophys. Res. 93, 9883–9892. https://doi.org/10.1029/JA093iA09p09883.

Liu, J.Y., Chen, Y.Y., Tsai, H.F., 2010, Developments of Ionospheric Climate Model and Space Weather Monitoring by Using FORMOSAT-3/COSMIC Data): Remark 1 – OSSE of 2-D Photometer Tomography on F7/C2. Workshop on Formosa 3 Results and Formosa 7 Future Projects and Collaborations – GPSARC retreat, Tao-Yuan, Taiwan, Dec 27, 2010.

Liu, J.Y., Rajesh, P.K., Lee, I.T., Chow, T.C., 2011. Airglow observations over the equatorial ionization anomaly zone in Taiwan. Ann. Geophys. 29, 749–757. https://doi.org/10.5194/angeo- 29-749-2011.

Mendillo, M., Baumgardner, J., Nottingham, D., Aarons, J., Reinisch, B., Scali, J., Kelley, M., 1997. Investigations of thermospheric-ionospheric dynamics with 6300-Å images from the Arecibo Observatory. J. Geophys. Res. 102 (A4), 7331–7343. https://doi.org/10.1029/96JA02786.

Nelson, G.J., Cogger, L.L., 1971. Dynamical behavior of the nighttime ionosphere at Arecibo. J. Atmos. Sol. Terr. Phys. 33, 1711–1726.

Peterson, V.L., Van Zandt, T.E., Norton, R.B., 1966. F-region nightglow emissions of atomic oxygen, 1. Theory. J. Geophys. Res. 71, 2255–2265. https://doi.org/10.1029/JZ071i009p02255.

Porter, H.S., Silverman, S.M., Tuan, T.F., 1974. On the behavior of airglow under the influence of gravity waves. J. Geophys. Res. 79 (25), 3827–3833. https://doi.org/10.1029/JA079i025p03827.

Rajesh, P.K., Liu, J.Y., Chiang, C.Y., Chen, A.B., et al., 2009. First results of the limb imaging of 630.0 nm airglow using FORMOSAT-2/imager of sprites and upper atmospheric lightnings. J. Geophys. Res. 114, A10302. https://doi.org/10.1029/2009JA014087.

Rajesh, P.K., Liu, J.Y., Sinha, H.S.S., Banerjee, S.B., 2010. Appearance and extension of airglow depletions. J. Geophys. Res. 115, A08318. https://doi.org/10.1029/2009JA014952.

Rajesh, P.K., Chen, C.H., Lin, C.H., Liu, J.Y., et al., 2014. Low-latitude midnight brightness in 630.0 nm limb observations by FORMOSAT-2/ISUAL. J. Geophys. Res. Space Phys. 4894–4904, 119. https://doi.org/10.1002/2014JA019927.

Yeh, T.L., Dmitriev, Alexei, Chu, Y.H., Jiang, S.B., Chen, L.W., 2012, NCU-SWIP space weather instrumentation payload – intelligent sensors on efficient real-time distributed LUTOS. In: 40th COSPAR Scientific Assembly. Held 2–10 August 2014, in Moscow, Russia, paper C0.2-10-14.